JOURNAL OF GEOPHYSICAL RESEARCH, VOL. 88, NO. C3, PAGES 1745–1759, FEBRUARY 28, 1983

Monte Carlo Simulations for Studying the Relationship Between Ocean Wave and Synthetic Aperture Radar Image Spectra

WERNER ALPERS

Institut für Geophysik, Universität Hamburg and Max-Planck-Institut für Meteorologie, Hamburg, Federal Republic of Germany

A theoretical model previously developed for describing the imaging of monochromatic ocean waves by synthetic aperture radar (SAR) is extended to relate ocean wave spectra to SAR image spectra. Since the SAR response to the moving ocean surface is nonlinear for a large range of ocean wave parameters, this relationship can, in general, not be described by a linear mapping transfer function. SAR image spectra are calculated from given ocean wave spectra by applying Monte Carlo simulation techniques. The computer simulations are performed with varying SAR parameters and for a unidirectional wave field propagating in azimuth direction. Though the model calculations are only one dimensional, they reveal the following basic features of the SAR imaging mechanism: (1) If the nonlinearity of the imaging is sufficiently strong, then the peak of the SAR image spectrum is shifted towards lower azimuthal wave numbers. (2) One parameter suitable for characterizing the degree of nonlinearity is the average velocity bunching parameter $\bar{c}$, which for SEASAT-SAR is given by $\bar{c} = 1.6 \times 10^3 \lambda_m^{-3/2} H_s \cos \phi$, where λ_m is the dominant wavelength and H_s the significant waveheight in meters, and ϕ the azimuth angle ($\phi = 0$ for azimuthally traveling waves). (3) The amount of the azimuthal shift of the spectral peak depends on $\bar{c}$, SAR integration time, and on the width of the ocean wave spectrum. It increases with integration time and spectral width. (4) In case of a fully developed wind sea, shifts of spectral peaks toward lower azimuthal wave numbers become significant for SEASAT-SAR if $\bar{c} \geq \pi/2$. For $\bar{c} \approx \pi$, the relative azimuthal wavenumber shift is of the order of $\frac{1}{2}$. If $\bar{c} \geq 2\pi$, the peak of the image spectrum is located near zero wave number and no wave information can be extracted from the SEASAT-SAR image spectrum.

1. INTRODUCTION

The imaging of ocean surface waves by synthetic aperture radar (SAR) has been the subject of many recent theoretical investigations [*Larson et al.*, 1976; *Elachi and Brown*, 1977; *Jain*, 1978; *Raney and Lowry*, 1976; *Tomiyasu*, 1978; *Raney and Shuchman*, 1978; *Alpers and Rufenach*, 1979; *Swift and Wilson*, 1979; *Raney*, 1980; *Valenzuela*, 1980; *Harger*, 1980; *Alpers and Rufenach*, 1980; *Rufenach and Alpers*, 1981; *Alpers et al.*, 1981; *Raney*, 1981].

In almost all of these investigations, only the special case of imaging one monochromatic ocean wave has been considered. Therefore, these SAR imaging theories apply primarily to narrow band swell systems. But, when the spectrum of the ocean surface wave field is broadband, then the previously developed theories suffice to describe the SAR imaging of the ocean wave field only if the imaging is a linear process. In this case the superposition principle holds and the mapping can be described by a linear mapping transfer function [*Alpers et al.*, 1981].

However, often the SAR imaging process is not linear because the ocean surface is moving. These motion induced nonlinearities in the imaging process are most severe for waves traveling in flight or azimuth direction. In the present paper we investigate how these nonlinearities affect the relationship between ocean wave and the SAR image spectrum.

It is well known that sometimes SAR does not detect ocean waves, although their wavelength is several times the spatial resolution [*Gonzales et al.*, 1979; *Kasischke*, 1980]. There is experimental evidence that nondetection is not confined to low waveheights. If this would be the case, then nondetection could easily be explained by a too low signal-to-noise or signal-to-clutter ratio [see, e.g., *Alpers and Hasselmann*, 1982]. However, it has been pointed out by *Alpers et al.* [1981] that image distortions due to nonuniform scatter motions may also lead to nonimaging. This occurs when the waves have a large azimuthal component and when their height exceeds a certain value.

In the following paper, we present model calculations based on Monte Carlo methods to relate SAR image to ocean wave spectra. Our model is one dimensional, which means that all waves travel in one direction. We restrict the model calculations to azimuthally traveling waves, because the effect of orbital motions on SAR imagery is largest for these waves.

Extending the model to a two-dimensional wave field is straightforward, but requires much more computing time. Such a two-dimensional SAR simulation study is required when investigating, for example, the directional spread of SAR image spectra, but this will not be treated in the present analysis.

The purpose of this paper is to elucidate the basic features of the ocean wave spectrum–SAR image spectrum relationship. In a subsequent paper a detailed comparison between calculated and measured two-dimensional SAR spectra will be given.

The procedure of the model calculations is outlined in section 2. In section 3 we describe how the ocean surface is modeled, and in section 4 we state the formulas used for describing the SAR imaging mechanism. The parameters used in the present computer runs are given in section 5, and some examples of Monte Carlo runs are presented in section 6. Finally, in section 7 we discuss and summarize the results obtained from the Monte Carlo calculations.

Paper number 2C1118.
0148-0227/83/002C-1118$05.00

2. OUTLINE OF THE MODEL CALCULATIONS

The model calculations consist of the following steps:

1. Generate one realization of a statistical ocean surface wave field with a given spectrum by using Monte Carlo techniques.
2. Calculate the orbital velocity and acceleration in range direction, as well as the 'real' cross section modulation for each facet on the ocean surface.
3. Calculate the SAR image of this particular realization of the ocean wave field by applying the SAR imaging mechanism for moving scatterers as discussed previously by *Raney* [1971], *Alpers and Rufenach,* [1979], *Swift and Wilson* [1979], *Rufenach and Alpers* [1981], and *Alpers et al.* [1981].
4. Calculate the 'instantaneous' autospectra and coherence function of the ocean wave field and its SAR image.
5. Generate more realizations of the ocean wave field and repeat the above calculations.
6. Calculate the average autospectra and the coherence function.
7. Compare the average ocean wave field spectrum with the SAR image spectrum and calculate the linear modulation transfer function as well as the spectral mapping function.

These calculations are carried out for a variety of ocean wave spectra, including fully developed wind sea and swell spectra. Where applicable, the SEASAT-SAR parameters are inserted [see, e.g., *Jordan,* 1980].

3. REPRESENTATION OF THE OCEAN SURFACE WAVE FIELD

We approximate the ocean wave field by a superposition of a finite number of harmonic components

$$\zeta(\mathbf{x}_0, t) = \sum_{i=1}^{N} z(\mathbf{k}_i) \cos(\mathbf{k}_i\mathbf{x}_0 - \omega_i t + \phi_i) \tag{1}$$

$\mathbf{k}_i$ and ω_i denote the two-dimensional wave vector and frequency of the ith wave component. $\zeta(\mathbf{x}_0, t)$ is the wave-height, which is a function of the two-dimensional space coordinate $\mathbf{x}_0$ and time t. The amplitudes $z(\mathbf{k}_i) = |z(\mathbf{k}_i)|$ and phases ϕ_i are random variables with Rayleigh and uniform probability distribution functions, respectively.

The $z(\mathbf{k}_i)$ are related to the ocean surface wave spectrum $E(\mathbf{k}_i)$ by

$$\langle z(\mathbf{k}_i) z(\mathbf{k}_j) \rangle = 2\delta_{ij} E(\mathbf{k}_i) \Delta\mathbf{k} \tag{2}$$

where $\Delta\mathbf{k} = k_{i+1} - \mathbf{k}_i$ is the stepwidth (which is assumed to be independent of i), δ_{ij} the Kronecker symbol ($\delta_{ij} = 1$ for $i = j$ and $\delta_{ij} = 0$ for $i \neq j$), and $\langle \cdots \rangle$ and ensemble average over different realizations of the ocean wave field. Likewise, the ensemble average of the product of the ϕ_i is given by

$$\langle \phi_i \phi_j \rangle = \frac{\pi^2}{3} \delta_{ij} \tag{3}$$

The Monte Carlo simulation consists in generating random values for the amplitudes $z(\mathbf{k}_i)$ and phases ϕ_i such that the $z(\mathbf{k}_i)$ are Rayleigh and the ϕ_i uniformly distributed and their second statistical moments are given by equations (2) and (3).

We restrict the present analysis to a unidirectional wave field and assume that it can be described by a one-dimensional JONSWAP-type spectrum [*Hasselmann et al.,* 1973, 1976]

$$E(k, \phi) = E(k)\delta(\phi - \phi_0) \tag{4a}$$

with

$$E(k) = E_{PM}(k) \exp\left\{\ln \gamma \exp\left[-\frac{1}{\sigma^2}\left(\left(\frac{k}{k_m}\right)^{1/2} - 1\right)^2\right]\right\} \tag{4b}$$

where $E_{PM}(k)$ is the one-dimensional Pierson-Moskowitz spectrum

$$E_{PM}(k) = \frac{\alpha}{2} k^{-3} \exp\left\{-\frac{5}{4}\left(\frac{k}{k_m}\right)^{-2}\right\} \tag{5}$$

and δ the Direac delta function. Here $k = |\mathbf{k}| = 2\pi/\lambda$ denotes the modulus of the wave vector $\mathbf{k}$, λ the wavelength, k_m the wave number of the spectral peak, α the Phillips parameter, γ the peak enhancement factor (which is the ratio of the peak value of the corresponding Pierson-Moskowitz spectrum with the same values of k_m and α), and σ a shape parameter that specifies the width of the spectral peak and which is defined by $\sigma = \sigma_a$ for $k \leq k_m$ and $\sigma = \sigma_b$ for $k > k_m$.

If the spectrum describes a growing wind sea, then, according to *Hasselmann et al.* [1973, 1976] the parameters σ_a, σ_b, and γ have the values $\sigma_a = 0.07$, $\sigma_b = 0.09$, and $\gamma = 3.3$. For a fully developed wind sea, the JONSWAP spectrum reduces to the Pierson-Moskowitz spectrum. In this case, is $\gamma = 1$ and $\alpha = 0.0081$. The peak wave number k_m is then equal to the Pierson-Moskowitz wave number k_{PM}, which is related to the local wind speed U_{10} at a height of 10 m by

$$k_m = 2\pi/\lambda_m = k_{PM} = 0.67g/U_{10}^2 \tag{6}$$

where g is the gravitational constant and λ_m the dominant wavelength.

For a fully developed wind sea, the significant wave height H_s is related to the wind speed U_{10} by

$$H_s = 0.24U_{10}^2/g \tag{7}$$

In this paper we use the JONSWAP spectrum also to describe swell. This is done by choosing a large peak enhancement factor $\gamma(\gamma > 3.3)$ and a small Phillips constant $\alpha(\alpha < 0.0081)$.

4. SAR IMAGING PROCESS

According to *Alpers and Rufenach* [1979], *Rufenach and Alpers* [1981], and *Alpers et al.* [1981], the ensemble-averaged image intensity $I(x, y)$ of a monochromatic ocean wave (after range compression) can be expressed by the following integral

$$I(\mathbf{x}) = B \int_{-\infty}^{\infty} \sigma(\mathbf{x}_0)\rho_{aN}/\rho'_{aN}(\mathbf{x}_0) \exp\left\{-\pi^2/\rho'_{aN}(\mathbf{x}_0)^2 \cdot \left[x - x_0 - \frac{R}{V} u_r(\mathbf{x}_0)\right]^2\right\} \delta(y - y_0)\, dx_0\, dy_0 \tag{8}$$

Here $\sigma(\mathbf{x}_0)$ denotes the radar cross section that varies along the long ocean wave profile due to tilt and hydradynamic modulation, ρ_{aN} the stationary target azimuthal resolution for N (incoherent) looks, ρ'_{aN} the degraded azimuthal resolution due to target acceleration and finite scene coherence

time, R the distance between the target and the radar (range), V the platform velocity, and u_r the orbital velocity in look direction of the antenna (we define the positive direction here as pointing towards the antenna). $\mathbf{x}_0 = (x_0, y_0)$ and $\mathbf{x} = (x, y)$ are the Cartesian coordinates on the ocean surface and the SAR image, respectively. x_0 and x are the azimuthal (along track) components. B is a constant which depends on the parameters of the SAR system, including the SAR correlator. The value of B is irrelevant for the present analysis since we are interested in relative changes of $I(\mathbf{x})$.

In deriving the above integral representation of the ensemble-averaged image intensity, the following simplifying assumptions have been made: (1) $\omega T/2 \lesssim 1$, where ω is the radian frequency of the ocean wave and T the coherent integration time. (2) The scattering at the ocean surface can be described as the scattering at an ensemble of scatter elements (facets) which are statistically independent. (3) The SAR antenna has a Gaussian antenna pattern in azimuth direction. (4) Range-azimuth coupling can be neglected in SAR processing. (5) The SAR is a perfect instrument that maps uniquely a time-invariant two-dimensional radar cross section distribution $\sigma(\mathbf{x}_0)$ into an image intensity distribution $I(\mathbf{x})$. The system transfer function is a constant in the wave number range considered here. (6) System noise and speckle do not limit the SAR resolution.

The degraded azimuthal resolution ρ'_{aN} is given by

$$\rho'_{an}(\mathbf{x}_0) = N\rho_a \left\{1 + \frac{1}{N^2}\left[\left(\frac{\pi T^2}{\lambda_0} a_r(\mathbf{x}_0)\right)^2 + \left(\frac{T}{\tau_s}\right)^2\right]\right\}^{1/2} \quad (9a)$$

$$= \left\{(N\rho_a)^2 + \left(\frac{\pi}{2}\frac{R}{V} a_r(\mathbf{x}_0) \cdot T\right)^2 + \left(\frac{\lambda_0 R}{2V\tau_s}\right)^2\right\}^{1/2} \quad (9b)$$

where

$$\rho_a = \frac{\lambda_0 R}{2TV} \quad (10)$$

is the maximum achievable (one-look, full-bandwidth) resolution, λ_0 the radar wavelength, τ_s the scene coherence time [*Rufenach and Alpers*, 1981], and $a_r(\mathbf{x}_0)$ the orbital acceleration in look direction of the antenna (range direction).

If the surface elevation associated with the long waves is given by equation (1), then the orbital velocity and acceleration in range direction at $t = 0$, are given by

$$u_r(\mathbf{x}_0) \equiv u_r(\mathbf{x}_0, t = 0) = \sum_{i=1}^{N} z(\mathbf{k}_i)\omega_i G(\theta, \phi) \cdot \sin(\mathbf{k}_i\mathbf{x}_0 + \delta + \phi_i) \quad (11)$$

$$a_r(\mathbf{x}_0) \equiv a_r(\mathbf{x}_0, t = 0) = -\sum_{i=1}^{N} z(\mathbf{k}_i)\omega_i^2 G(\theta, \phi) \cdot \cos(\mathbf{k}_i\mathbf{x}_0 + \delta + \phi_i) \quad (12)$$

where

$$G(\theta, \phi) = (\sin^2\theta \sin^2\phi + \cos^2\theta)^{1/2} \quad (13)$$

$$\delta = tg^{-1}(tg\theta \sin\phi) \quad (14)$$

and

$$\omega_i = \omega(\mathbf{k}_i) = (g|\mathbf{k}_i|)^{1/2} \quad (15)$$

Here θ denotes the radar incidence angle and ϕ the azimuth angle, which is at the angle between the propagation direction of the ocean wave and the satellite flight direction ($\phi = 0$ for azimuthally traveling waves). The variation in cross section due to tilt and hydrodynamic modulation can be written as [*Alpers and Hasselmann*, 1978]

$$\sigma(\mathbf{x}_0) = \sigma_0\left\{1 + \sum_{i=1}^{N} |R(\mathbf{k}_i)|\, z(\mathbf{k}_i) \cos(\mathbf{k}_i\mathbf{x}_0 + \phi_i - \psi_i)\right\} \quad (16)$$

where $|R(\mathbf{k}_i)|$ and ψ_i are the modulus and phase of the modulation transfer function, respectively. Formula (16) implies that cross section and ocean wave field are linearily related. It is often convenient to define a dimensionless modulation transfer function $\mathbf{m}(\mathbf{k})$ by

$$\mathbf{m}(\mathbf{k}) = |\mathbf{k}|^{-2}\, \mathbf{k}R(\mathbf{k}) \quad (17)$$

$\mathbf{m}$ can also be interpreted as the modulation transfer function that relates the ocean slope spectrum to the real aperture radar (RAR) image spectrum. (This function is essentially identical to the modulation transfer function m used by *Wright et al.* [1980]).

Equation (8) shows that in azimuth direction an image point receives contributions from several scatter elements (facets) on the ocean surface. These contributions are weighted by a Gaussian function. Its width is the azimuthal resolution, which varies with x_0. The main contributions to the integral (8) arise from those facets for which the argument of the Gaussian function in equation (8) vanishes:

$$x = x_0 + \frac{R}{V} u_r(\mathbf{x}_0) \quad (18)$$

For small orbital velocities, this equation has only one solution, which means that the SAR image is a one-to-one map of the imaged scene. However, for large orbital velocities, the equation may have multiple solutions, which implies that several facets on the ocean surface give major contributions to one particular image element. The SAR ocean wave imaging ceases to be a one-to-one mapping process. We expect already from these considerations that the transition from the unique to the multiple value solution of equation (18) constitutes the limit beyond which the SAR imaging of ocean waves becomes significantly nonlinear.

The mapping of a monochromatic ocean surface onto the SAR image plane is illustrated in Figure 1, where equation (18) is plotted in terms of the nondimensional quantities

$$x_0' = k_x x_0 \qquad x' = k_x x \quad (19)$$

and where $k_y y_0 + \delta$ has been set equal to zero. The resulting equation reads

$$x' = x_0' + c \sin x'_0 \quad (20)$$

with

$$c = \frac{R}{V}\zeta_0 \omega k_x G(\theta, \phi) \quad (21)$$

where ζ_0 is the wave amplitude.

This parameter c has been used previously by *Alpers and Rufenach* [1979] and *Alpers et al.* [1981] for describing the transition between linear and nonlinear imaging.

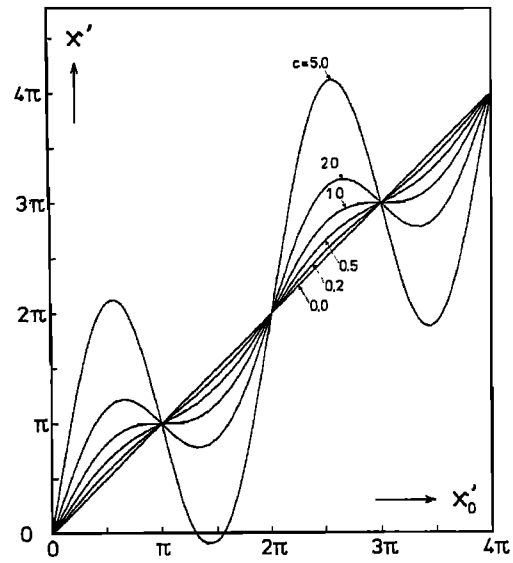

Fig. 1. Transformation of the azimuthal component of the ocean plane x_0' to the SAR image plane x' for different values of c (see equation (20)). For $c > 1$, the transformation is not unique.

If the deep water dispersion relation is applicable, then c can also be written as

$$c = \frac{R}{V}\zeta_0 g^{1/2}|\mathbf{k}|^{3/2}G(\theta, \phi)\cos\phi \tag{22}$$

where g is the gravitational constant.

Figure 1 shows plots of equation (20) for different values of c [see also *Raney*, 1981].

For example, if an ocean wave of wavelength $\lambda = 100$ m travels in azimuthal direction ($\phi = 0$) and is viewed by the radar at an incidence angle of $\theta = 20°$, and if $R/V = 128$ s (SEASAT), then $c = 0.2$, 0.5, 1.0, 2.0, and 5.0 correspond to $\zeta_0 = 0.03$, 0.08, 0.16, 0.34, and 0.84 m, respectively. However, if the wavelength is $\lambda = 200$ m, then the corresponding wave amplitudes are $\zeta_0 = 0.10$, 0.24, 0.48, 0.95, and 2.38 m, respectively.

The azimuthal density distribution of the backscatter elements in the SAR image is given by

$$D = \left|\frac{dx'}{dx_0'}\right|^{-1} = |1 + c\cos x_0'|^{-1} \tag{23}$$

The image of a long ocean wave contains regions, where, in an alternating way, the apparent position of the backscatter elements are concentrated (or bunched) and spread out. This phenomenon in SAR ocean wave imaging is also called velocity bunching [*Alpers and Rufenach*, 1979].

A radial target acceleration leads to a degraded azimuthal resolution $\rho'_{aN}(\mathbf{x}_0)$. The backscattered energy originating from one facet on the ocean surface is smeared in azimuth in the image. The degree of the smearing varies with azimuthal position on the long wave profile as indicated in Figure 2. Note, however, that the total backscattered energy is conserved (see equation (8)).

The azimuthal image smear is relatively large for SEASAT-SAR. For azimuthally traveling waves and $\theta = 20°$, the maximum degradation in one-look ($N = 1$) azimuthal resolution is in case of $\pi T^2\lambda_0^{-1} \cdot a_r^2 \gg 1$ and $\rho_a = 6.25$ m given by (see equation (9*a*))

$$d_a = \rho'_a/\rho_a \approx 4.4 \times 10^3\zeta_0/\lambda \tag{24}$$

This implies, for example, that for a monochromatic ocean wave of wavelength $\lambda = 200$ m and amplitude $\zeta_0 = 0.5$ m, the degraded azimuthal resolution varies between

$$\rho'_{a,\min} = \rho_a = 6.25 \text{ m} \tag{25a}$$

and

$$\rho'_{a,\max} = 12\rho_a = 69 \text{ m} \tag{25b}$$

From these considerations it is evident that the degradation in azimuthal resolution due to wave motions is an important factor in the imaging process for SEASAT-SAR. However, the azimuthal image smear becomes less important for SAR's with shorter integration times (see equation (9*b*)).

5. Parameters Used in the Calculations

In the present calculations we simulate SAR images that are 768 m long in azimuth direction and which have a pixel size of 6 m. Since, owing to target motions, the image field may be a map of a larger ocean field, the corresponding azimuthal ocean field length is extended at both ends to (768 + 2 × 198) m = 1164 m. In this way, one can account for maximum azimuthal shifts and image smear of 198 m.

We approximate the long ocean wave field by a sum of 30 terms with equidistant azimuthal wave number spacing $\Delta k_x = 2\pi/768$ m^{-1} (see equation (1)). The high wave wave number cutoff is at $k_{x,\max} = 0.242$ m^{-1}, corresponding to a wavelength of 26 m. The averaged spectra are obtained from 50 Monte Carlo runs (100 degrees of freedom).

In all calculations presented here we keep the parameters λ_0, ρ_a, θ, and ϕ fixed: $\lambda_0 = 0.23$ m, $\rho_a = 6.25$ m, $\theta = 20°$, $\phi = 0°$. In one set of Monte Carlo runs we vary R/V in order to

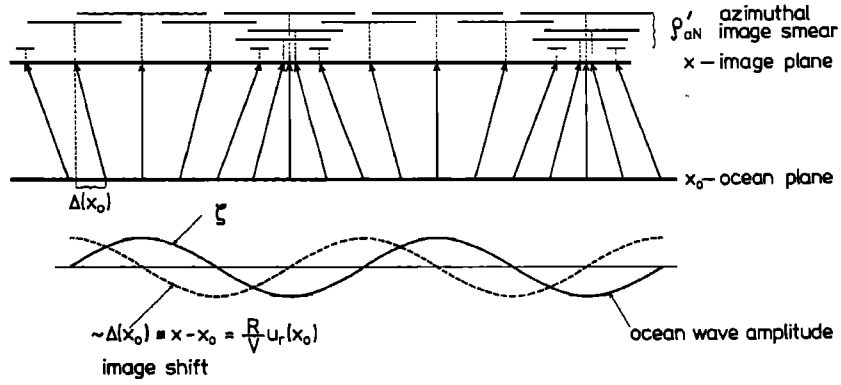

Fig. 2. Azimuthal image shift and image smear associated with a monochromatic ocean wave.

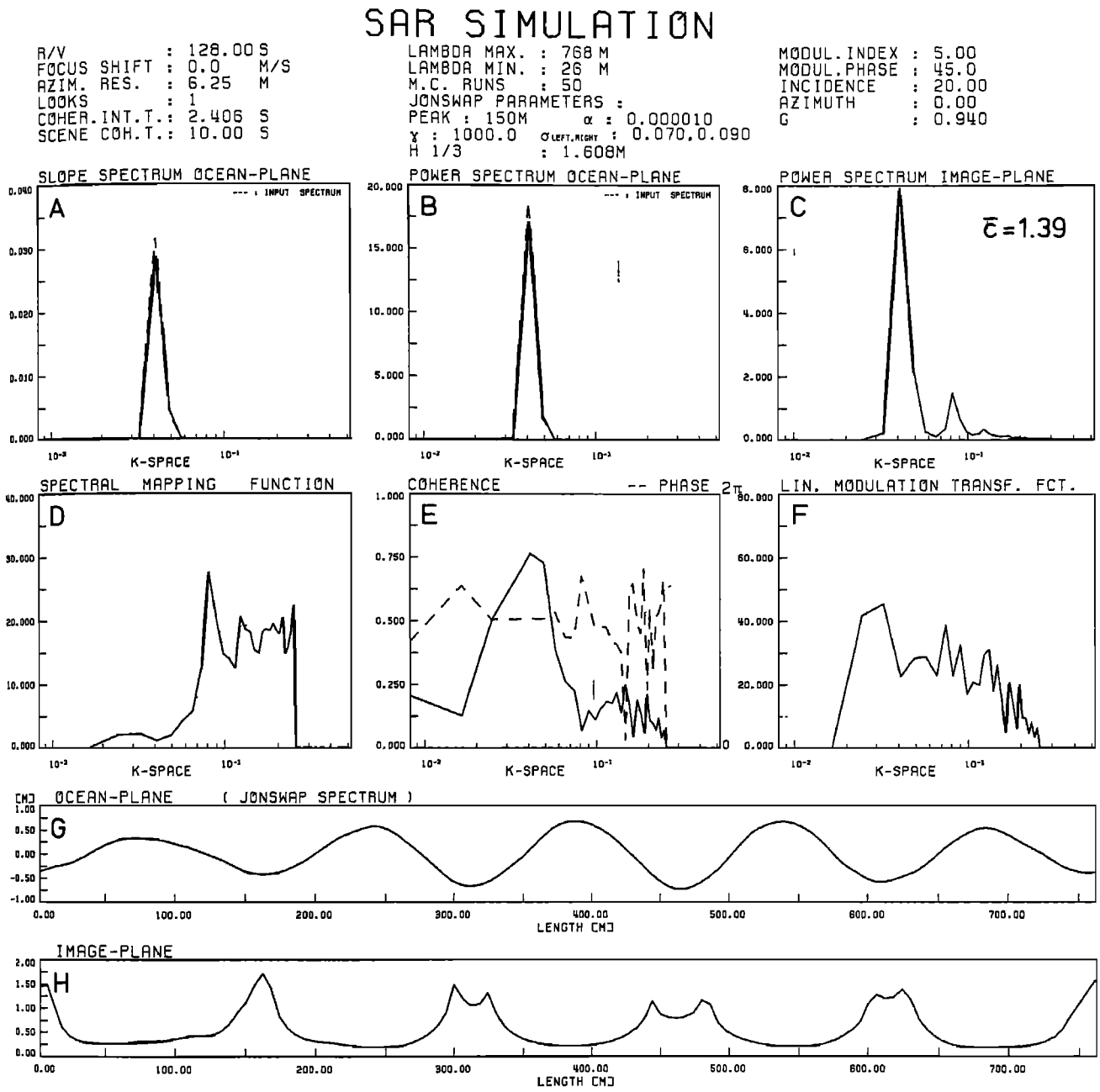

Fig. 3. Example of a Monte Carlo simulation run showing SEASAT-SAR imaging of a very narrow band swell of 150 m wavelength and 1.6 m significant waveheight traveling in azimuth direction. The heading states the radar and ocean wave parameters used in the run. The ocean wave spectrum is plotted as slope spectrum in panel A and as waveheight spectrum in panel B. The dotted line represents the ideal input spectrum and the solid line the actual input spectrum generated during this particular Monte Carlo run. Panel C shows the resulting SAR image spectrum with the parameter $\bar{c}$ defined by equation (29) as insert, panel D the spectral mapping function defined by equation (30), panel E the coherence function (modulus and phase) of the SAR image intensity and the waveheight, and panel F the linear modulation transfer function defined by equation (31). Panel G shows one realisation of the ocean wave field and panel H its SAR image.

study the effect of target motions on SAR ocean wave spectra. The scene coherence time is chosen as $\tau_s = 10$ s.

The shape parameters of the JONSWAP type spectra (see equation (4)) are set $\sigma_a = 0.07$ and $\sigma_b = 0.09$ in all runs, while the parameters α and γ are varied.

In all Monte Carlo runs presented in this paper, the 'real' cross-section modulation transfer function is chosen as $|m(k_i)| = 5$ and $\psi_i \equiv \psi(k_i) = \pi/4$. This is a typical value obtained from modulation experiments carried out from sea-based platforms [*Wright et al.*, 1980]. However, the principal results of this paper do not significantly depend on the specific value chosen for the real cross-section modulation transfer function, since in this paper we are mainly concerned with nonlinear effects which are due to motion effects. On the other hand, a detailed comparison of ocean wave spectra with SAR image spectra requires an exact knowledge of this transfer function.

6. Examples of Monte Carlo Runs

In total, more than 200 SAR simulation runs have been carried out on a CDC Cyber 173 computer. A sample is

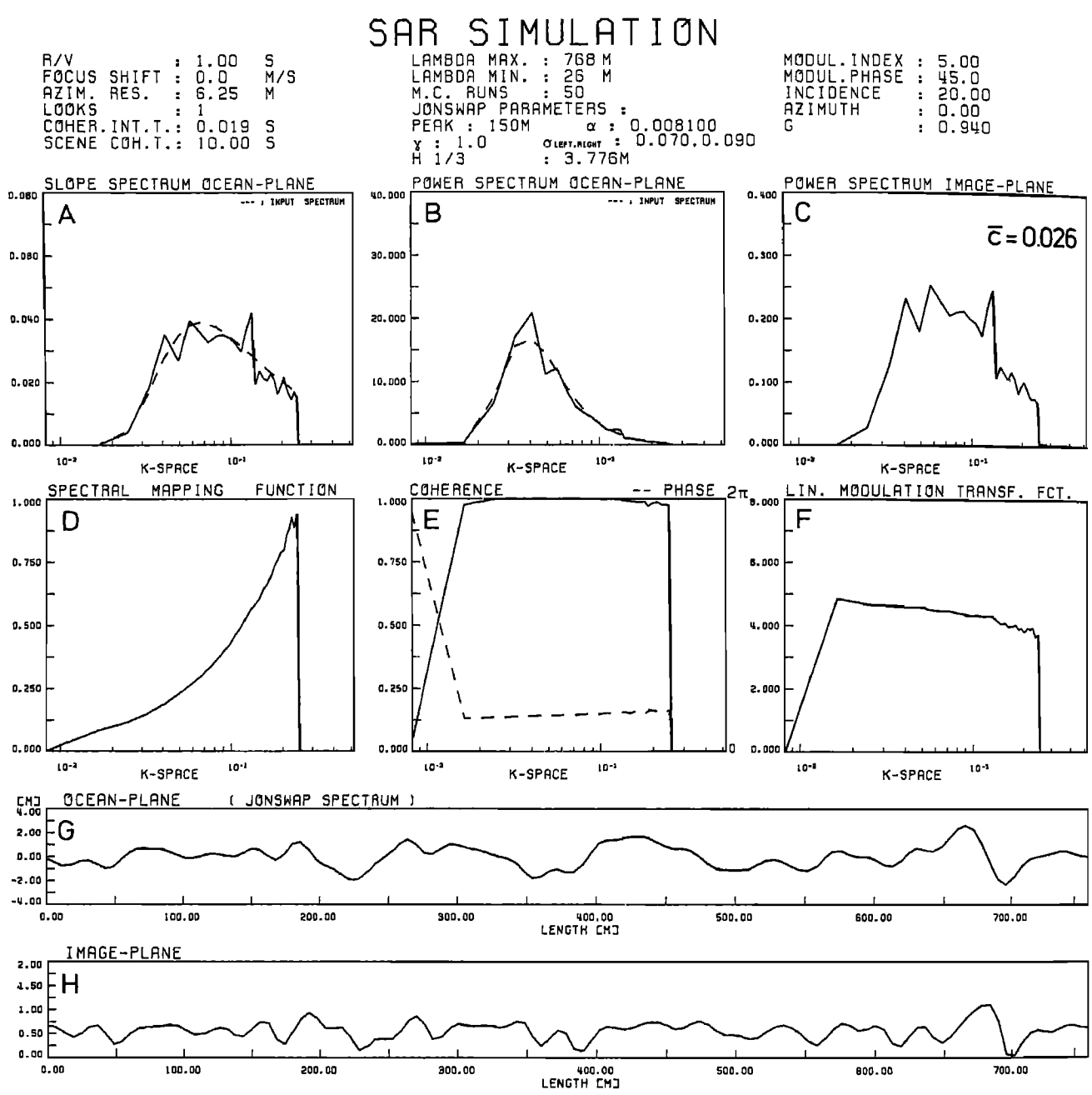

Fig. 4. SAR imaging with $R/V = 1$ s (R = target range, V = platform velocity) of azimuthally traveling waves having a Pierson-Moskowitz spectrum.

shown in Figures 3–12. These figures contain as headings the SAR, ocean wave, and modulation parameters used in the computer runs. Panel A shows the input spectrum plotted as slope spectrum $S(k)$ and panel B the same input spectrum plotted as waveheight spectrum $E(k)$. Both spectra are related by

$$S(k) = k^2 E(k) \tag{26}$$

The dashed line represents the ideal spectrum, while the solid line is the random spectrum generated during this particular Monte Carlo run.

The corresponding spectrum of the image intensity $F(k)$ is plotted in panel C in relative units ($B \cdot \sigma_0$ has been set equal to 1 (see equation (8) and (16))). Inserted in this figure is the velocity bunching parameter $\bar{c}$, which is one parameter characterizing the degree of nonlinearity of the imaging. This parameter is identical to the nondimensional parameter c defined by (22), if ζ_0 is replaced by $\langle\zeta^2\rangle^{1/2}$ and $|\mathbf{k}|$ by $|k_m|$. $\langle\zeta^2\rangle$ is the variance of the waveheight, which is related to the significant waveheight $H_s \equiv H_{1/3}$ by

$$4\langle\zeta^2\rangle^{1/2} = H_s \tag{27}$$

and $|k_m|$ the wave number at the peak of the spectrum. Thus, the definition of $\bar{c}$ is

$$\bar{c} = \frac{1}{4}\frac{R}{V} g^{1/2} G(\theta, \phi) \cos\phi |k_m|^{3/2} H_s \tag{28}$$

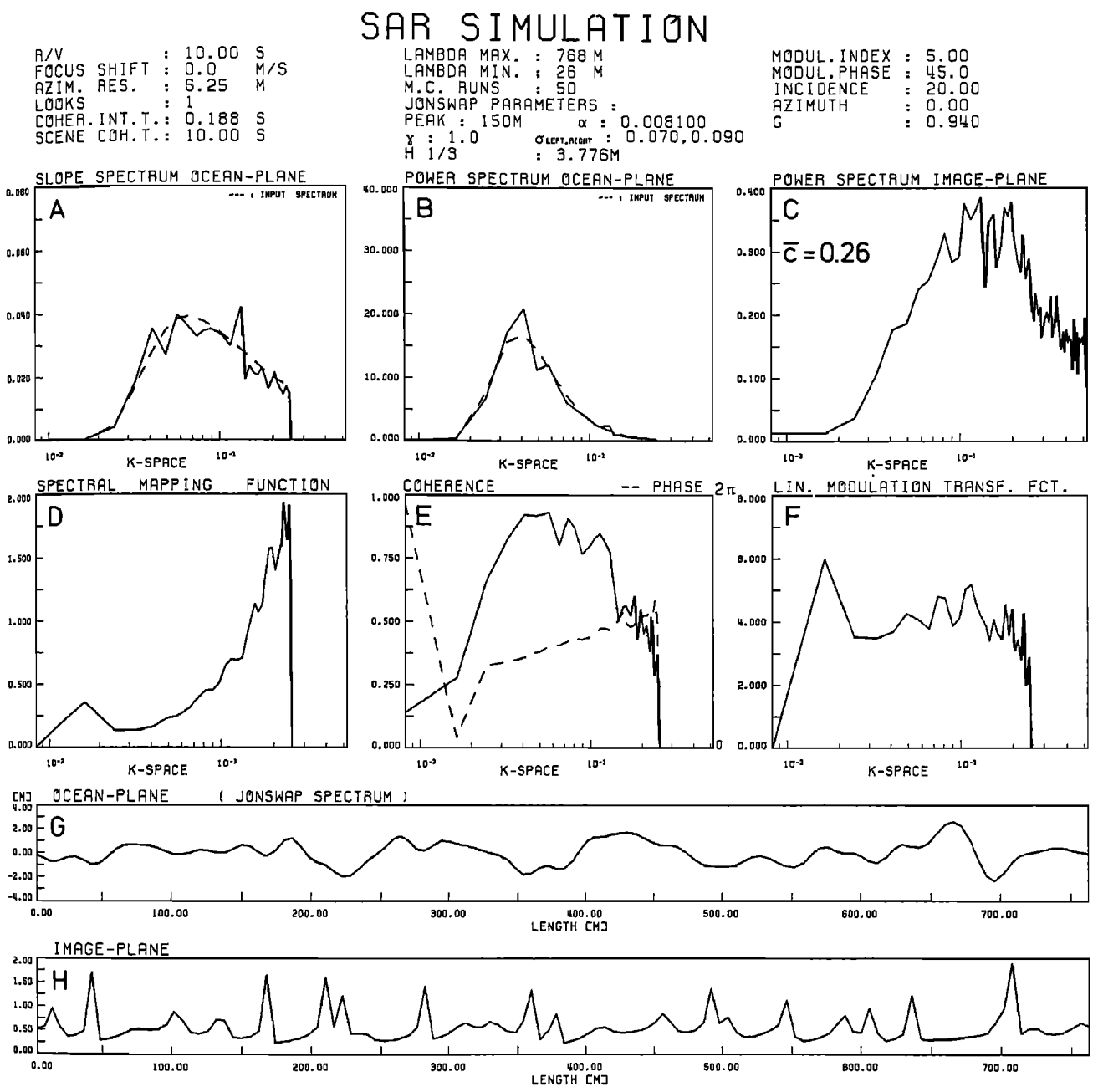

Fig. 5. SAR imaging with $R/V = 10$ s of azimuthally traveling waves having a Pierson-Moskowitz spectrum.

Inserting the SEASAT-SAR parameters and replacing $|k_m|$ by the dominant wavelength $\lambda_m = 2\pi|k_m|^{-1}$ yields

$$\bar{c}_{\text{SEASAT}} = 1.6 \times 10^3 \cos\phi\, \lambda_m^{-3/2} H_s \tag{29}$$

if λ_m and H_s are given in meters.

Panel D shows the spectral mapping function $T(k)$ defined by

$$T(k) = \bar{I}^{-1}\left(\frac{F(k)}{E(k)}\right)^{1/2} \tag{30}$$

where $\bar{I}$ is the average image intensity. $F(k)$ the image spectrum, and $E(k)$ the waveheight spectrum.

As stated before, the mapping is nonlinear for a large range of ocean wave parameters. If it were linear, then the appropriate way to describe the imaging process is by a linear modulation transfer function [*Bendat and Piersol*, 1966]. In this paper we define such function by

$$M(k) = |k|^{-1}\gamma(k)\bar{I}^{-1}\left(\frac{F(k)}{E(k)}\right)^{1/2} \tag{31}$$

where γ is the coherence function between the waveheight and the SAR image intensity. With this definition the modulation transfer function $M(k)$ becomes a dimensionless quantity. It is defined in analogy to the dimensionless 'real' cross-section modulation transfer function $\mathbf{m}(\mathbf{k})$ (see equation (17)). $|M(k)|$ is plotted in panel F.

The degree of linearity of the mapping can be characterized by $|\gamma(k)|$. A value of $|\gamma(k)|$ close to 1 means that the

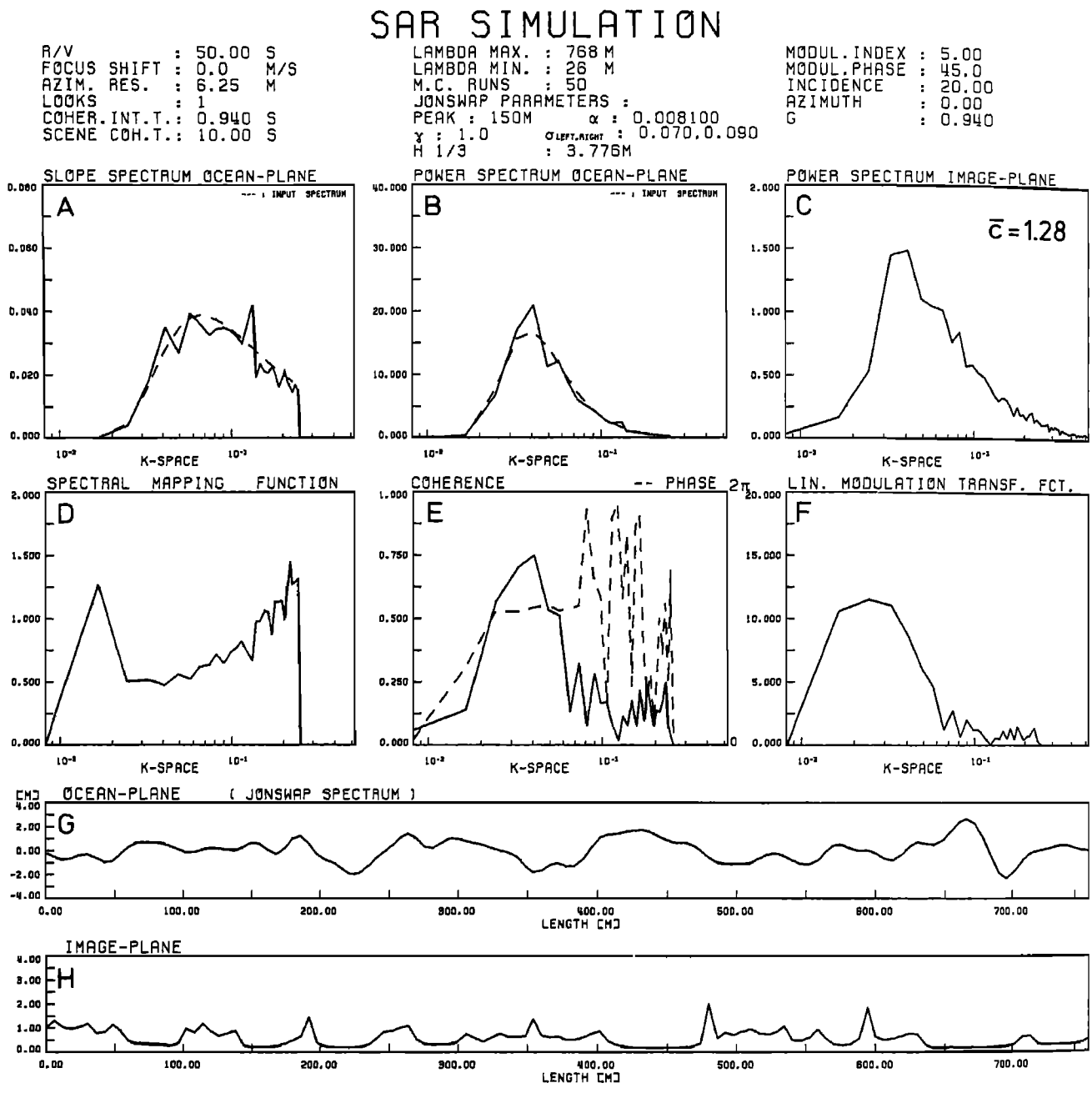

Fig. 6. SAR imaging with $R/V = 50$ s of azimuthally traveling waves having a Pierson-Moskowitz spectrum.

imaging is approximately linear, while a value close to 0 means that it is highly nonlinear. The modulus and phase of the coherence function are plotted in panel E. The left-hand scale applies for the modulus and the right-hand scale for the phase.

Finally, one realization of the ocean wave field generated during the simulation run is shown in panel G. The corresponding SAR image in relative units ($B \cdot \sigma_0 = 1$) is plotted in panel H.

Figure 3 shows SEASAT-SAR imaging of a narrow-band swell of 150 m wavelength and significant waveheight of 1.6 m propagating in azimuth direction. The nonlinearity of the mapping is evident from higher order peaks in the image spectrum at twice and three times the dominant wave number $k_m = 2\pi/150\ \mathrm{m}^{-1}$. Note that waveheight and SAR image intensity are out of phase by approximately 180 degrees.

Next, we investigate how the orbital motions affect the SAR image spectrum by varying the ratio R/V. Since we keep ρ_a constant, a small R/V ratio implies a short integration time (see equation (10)). For $R/V \rightarrow 0$, the SAR behaves like a real aperture radar (RAR), which is insensitive to target motions. Increasing the R/V ratio increases the influence of target motions on SAR imagery. We carry out the Monte Carlo calculations for a fully developed wind-sea with peak wave number $k_m = 2\pi/150\ \mathrm{m}^{-1}$, which corresponds to a wind speed of $U_{10} = 12.5\ \mathrm{m\ s}^{-1}$ (see equation (6)). The wave field is described by a JONSWAP spectrum with $\alpha = 0.0081$ (Phillips constant) and $\gamma = 1$. Figures 4–7 show runs with $R/V = 1$, 10, 50, and 128 s corresponding to $\bar{c} = 0.026$, 0.26,

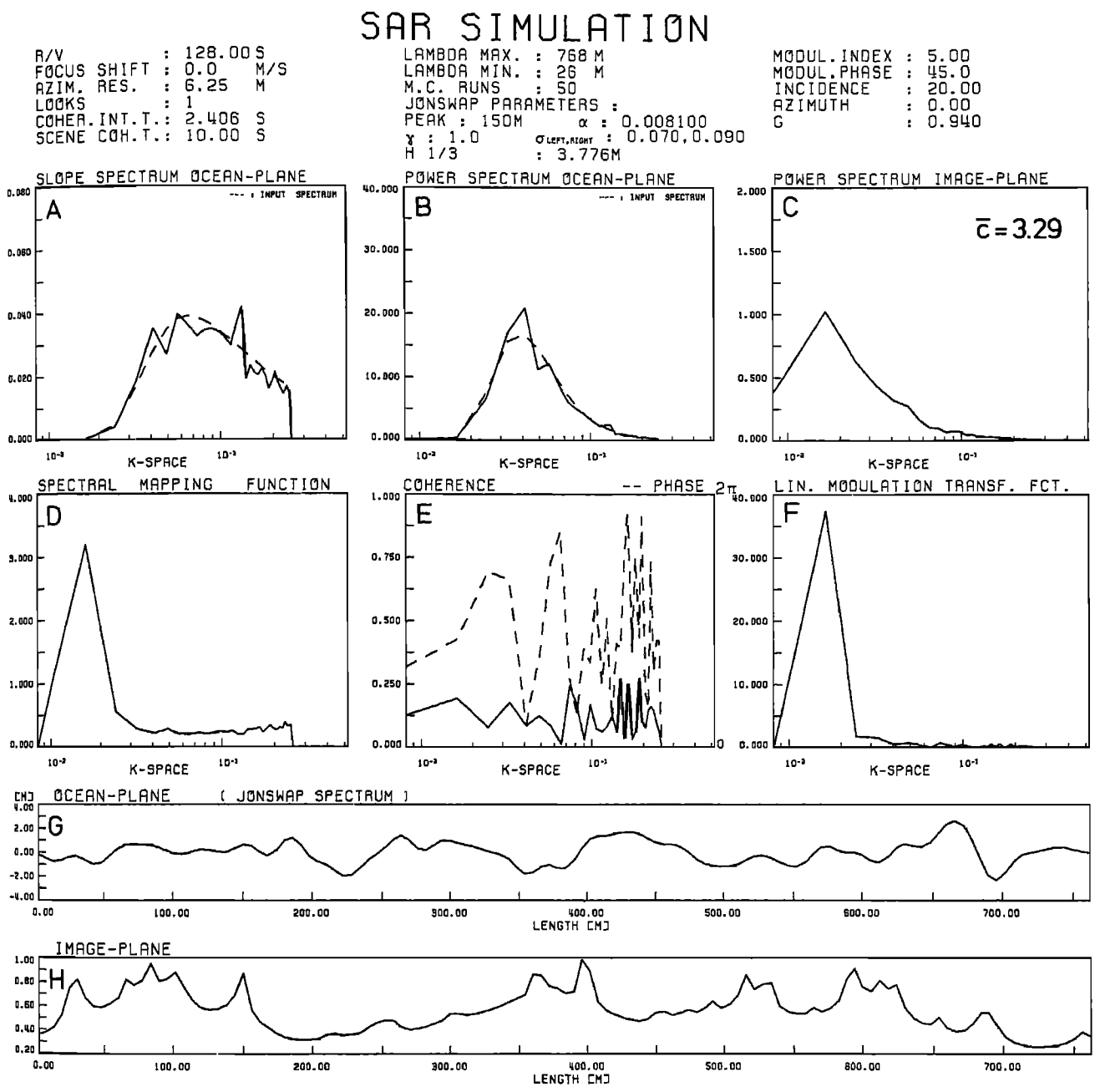

Fig. 7. SAR imaging with R/V = 128 s (SEASAT value) of azimuthally traveling waves having a Pierson-Moskowitz spectrum.

1.29, and 3.29, respectively. R/V = 1 s practically corresponds to RAR imaging. R/V = 10 s is a typical value for a fast and low flying airplane, and R/V = 50 s for a propeller research aircraft (e.g., the NASA CV 990 research aircraft). R/V = 128 s applies for SEASAT.

For $\bar{c}$ = 0.026 (R/V = 1 s, Figure 4) and $\bar{c}$ = 0.26 (R/V = 10 s, Figure 5) the coherence is 1 or close to 1 for a relatively large range of wave numbers. This means that the relationship between ocean waveheight and SAR image intensity is to a good approximation linear. For $\bar{c}$ = 0.026 the linear modulation transfer function M is almost equal to the dimensionless 'real' cross section linear modulation transfer function m. The slope spectrum and image spectrum have therefore their peaks at the same wavenumber. For $\bar{c}$ = 0.26 (Figure 5) the motion induced 'artificial' cross section modulation (velocity bunching) already contributes significantly to the imaging as can be seen, for example, from the phase of the coherence function which approaches 180 degrees for large k; 180 degrees is the phase of the velocity bunching modulation transfer function in case of linear imaging [see *Alpers et al.*, 1981]. The real cross section modulation transfer function is proportional to k, while the velocity bunching transfer function is proportional to $k^{3/2}$. This implies that velocity bunching contributes more to the modulation at higher wave numbers and that the peak of the image spectrum is shifted toward higher wave numbers.

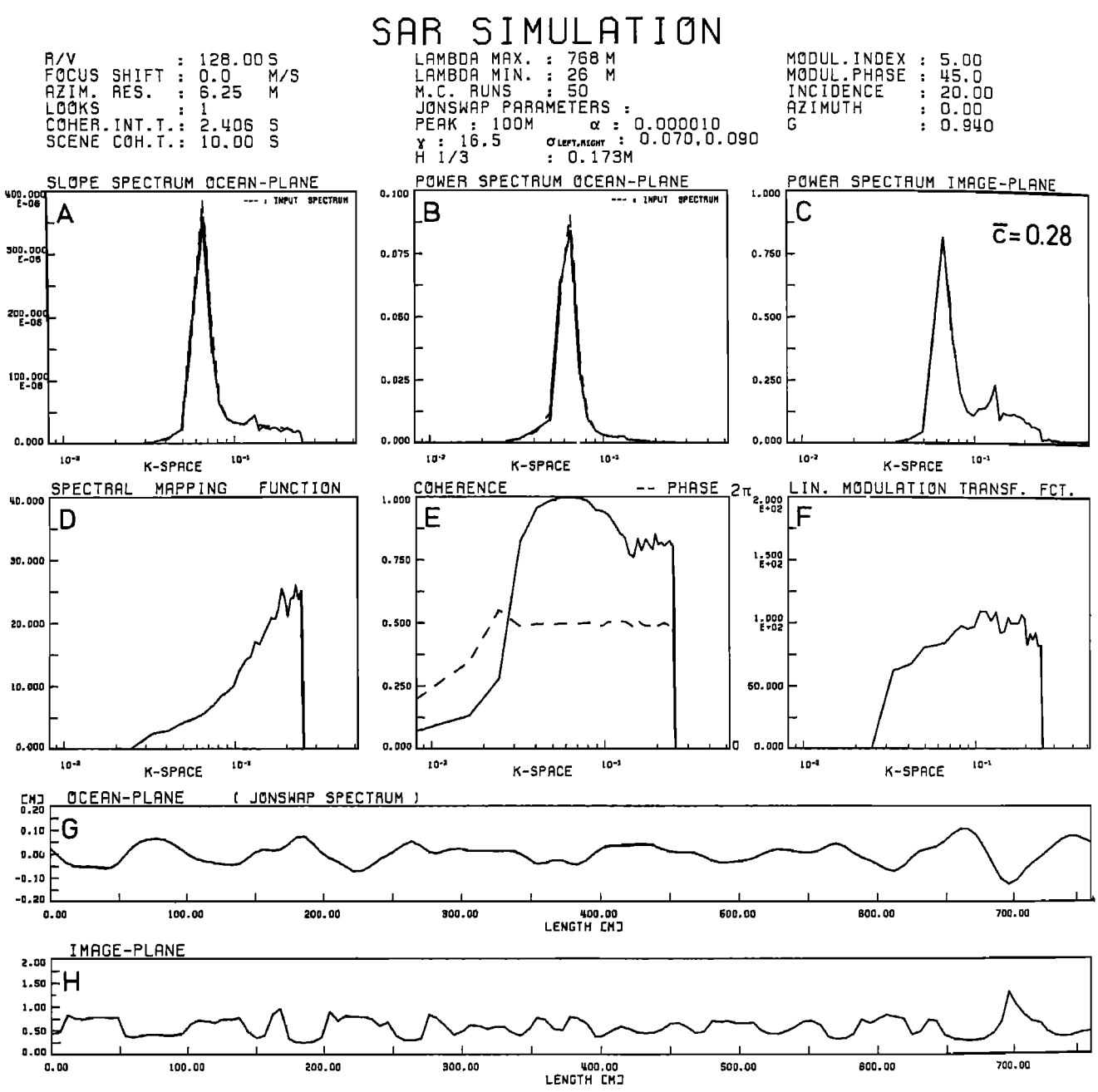

Fig. 8. SEASAT-SAR imaging of an azimuthally traveling swell of 100 m wavelength and 0.173 m significant waveheight.

For $\bar{c} = 1.29$ ($R/V = 50$ s, Figure 6) and $\bar{c} = 3.29$ ($R/V = 128$ s, Figure 7) the modulation is dominated by motion effects. In the latter case the coherence is very low, which implies a highly nonlinear mapping. The image spectrum now has more energy at lower wave numbers. In Figure 7 the peak of the image spectrum is at $k = 0.0164$ m^{-1} ($\lambda = 384$ m), while the peak of the waveheight spectrum is at $k = 0.041$ m^{-1} $\lambda = 153$ m).

Next we investigate how the imaging of a narrow-band wave system (swell) varies with waveheight H_s. In these runs the peak of the waveheight spectrum is fixed at $k_m = 2\pi/100$ m^{-1}.

Figures 8–12 show runs for $H_s = 0.173$ m ($\bar{c} = 0.28$), $H_s = 1.096$ m ($\bar{c} = 1.75$), $H_s = 1.73$ m ($\bar{c} = 2.77$), $H_s = 2.45$ m ($\bar{c} = 3.92$), and $H_s = 4.90$ m ($\bar{c} = 7.84$). In the first case ($\bar{c} = 0.28$, Figure 8), the imaging is quite linear, and the linear modulation transfer function is of the order of 100. For $\bar{c} = 1.75$ (Figure 9) the linear modulation has decreased, but still accounts for an appreciable part of the total modulation (the coherence is approximately 0.7 around the spectral peak). If $\bar{c}$ is increased further to $\bar{c} = 2.77$ (Figure 10), then the peak of the SAR image spectrum is shifted from $k = 0.065$ m^{-1} ($\lambda = 96$ m) to $k = 0.049$ m^{-1} ($\lambda = 128$ m). For $\bar{c} = 3.92$ (Figure 11) the image spectrum has a broad peak around $k = 0.0245$ m^{-1} ($\lambda = 256$ m) and for $\bar{c} = 7.84$ (Figure 12) around D.C. ($k = 0$ m^{-1}).

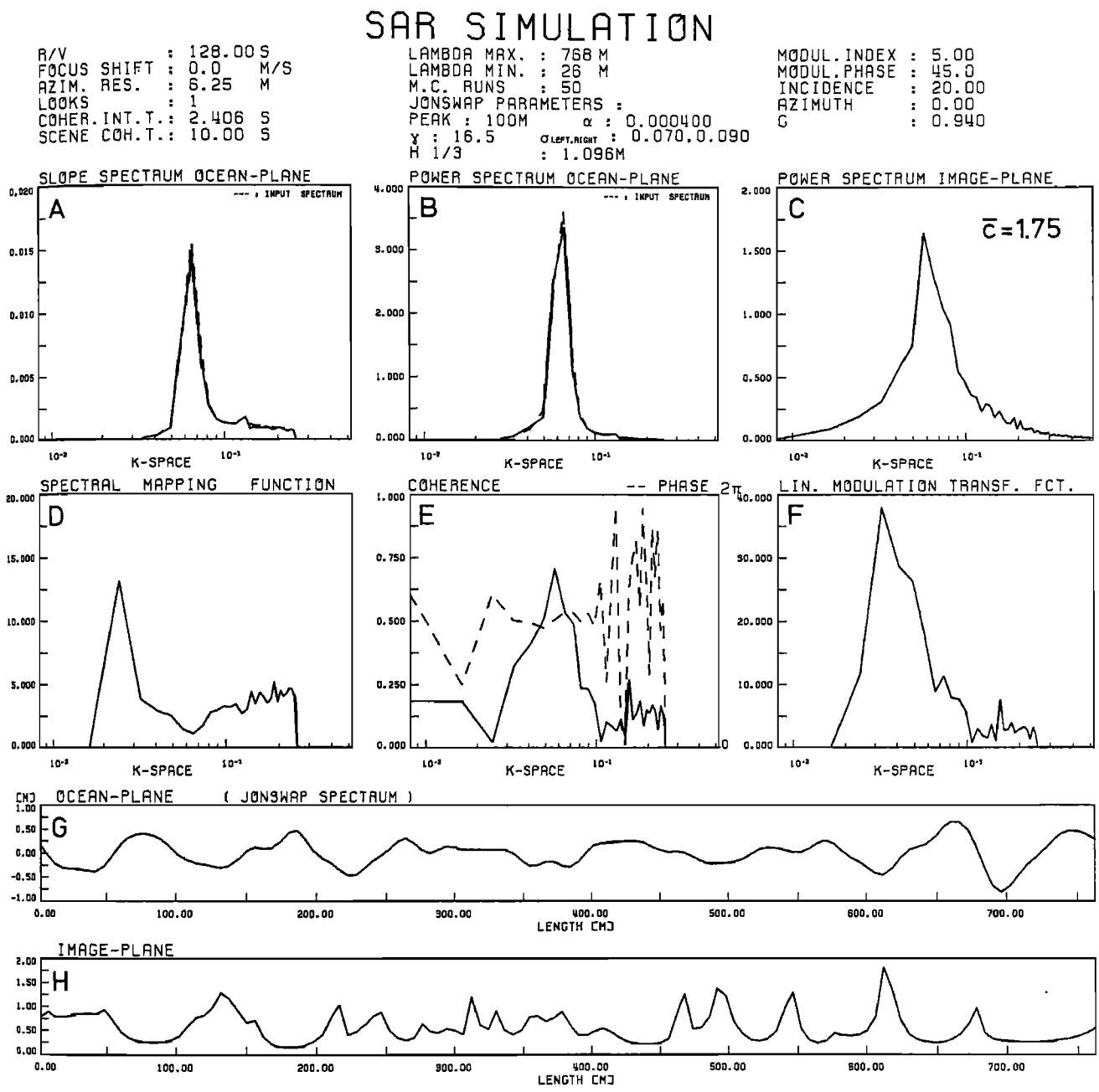

Fig. 9. SEASAT-SAR imaging of an azimuthally traveling swell of 100 m wavelength and 1.096 m significant waveheight.

7. Discussion

As can be seen from the examples of SAR simulation runs presented in the preceding section, the SAR response to the moving ocean wave field is nonlinear for a large range of ocean wave parameters. The nonlinearity is caused by an excessive velocity bunching as well as by an excessive azimuthal image smear (degradation in azimuthal resolution). The first effect depends on the R/V ratio and is independent of radar wavelength λ_0 and integration time T, while the second effect depends on T (see equation (9)).

A useful parameter for characterizing the degree of nonlinearity of a given SAR system is the velocity bunching parameter $\bar{c}$ defined by equation (28). However, how the nonlinearity of the mapping affects the ocean wave spectrum–SAR image spectrum relationship depends also on the value of the azimuthal image smear (which is proportional to SAR integration time) and on the width of the ocean wave spectrum.

The results from all Monte Carlo runs carried out so far can be summarized as follows: If the ocean wave spectrum is broadband, as in case of a wind sea, then for sufficiently large values of the nonlinearity parameter $\bar{c}$ the peak of the corresponding SAR image spectrum is shifted toward lower wave numbers. The motion of the sea surface thus turns the

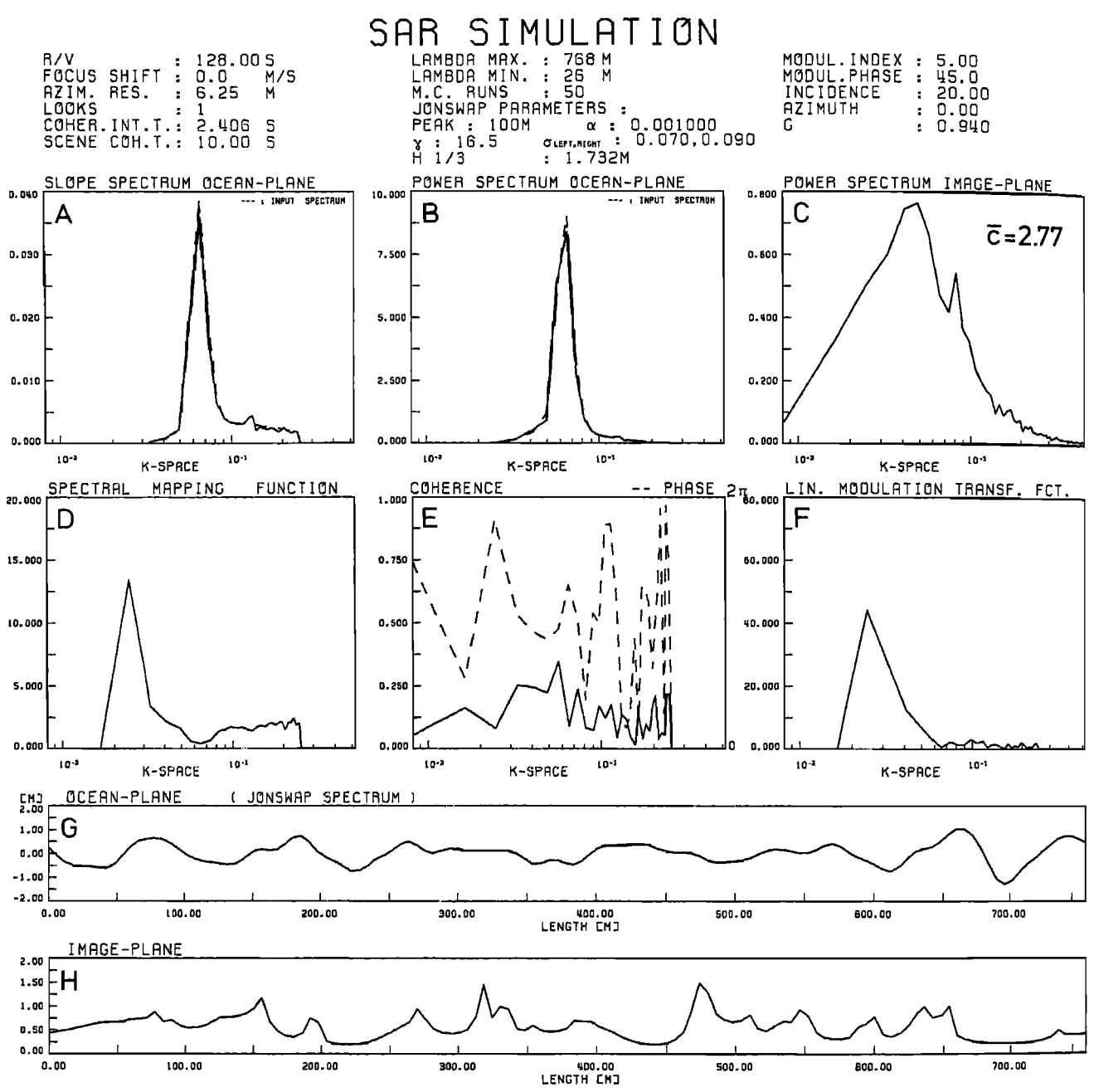

Fig. 10. SEASAT-SAR imaging of an azimuthally traveling swell of 100 m wavelength and 1.732 m significant waveheight.

SAR into a nonlinear imaging device. It is well known that the output signal of nonlinear systems contains in general frequencies that are multiple sums and differences of the frequencies present in the input signal. Nonlinear systems have the capability of frequency conversion (upward or downward), which means that energy can be transfered from one frequency band to another. In the present case of a SAR responding to a moving ocean wave field, the structure of the nonlinearity is such that the net effect is a shift of the spectral peak toward lower spatial frequencies and a distortion of the shape of the spectrum (spectral broadening).

The value of the shift and the degree of distortion depends on the form of the ocean wave spectrum and on SAR integration time. The shift is larger for broadband spectra (wind sea) than for narrow-band spectra (swell) and for SAR's with longer integration times.

In case of SEASAT-SAR and a Pierson-Moskowitz spectrum, shifts of spectral peaks toward lower wave numbers become significant if $\bar{c} > \pi/2$. The value $\bar{c} = \pi/2$ corresponds to an average maximum azimuthal image shift of $\lambda_m/4$ (see equation (19) and (20)). The condition $\bar{c} \leq \pi/2$ is fulfilled for wind speeds U_{10} above 27 m s^{-1} (see equations (6), (7), and (29)).

For $\bar{c} \approx \pi$ the shift is already so large that the peak of the

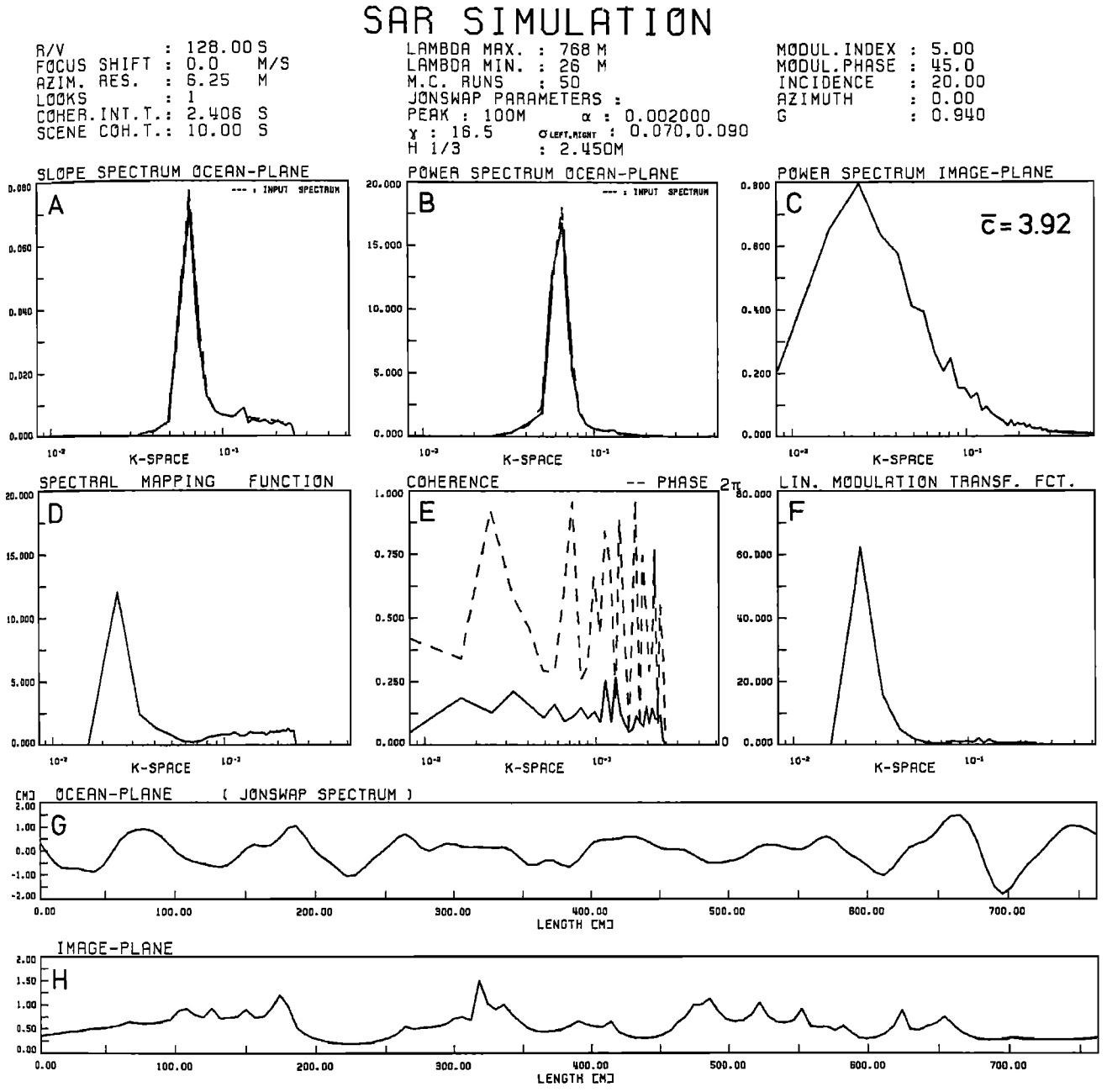

Fig. 11. SEASAT-SAR imaging of an azimuthally traveling swell of 100 m wavelength and 2.450 m significant waveheight.

image spectrum is located at approximately one half the wave number at which the waveheight spectrum has its maximum. Expressed in terms of wind speed this occurs for $U_{10} = 13.5$ m s^{-1}. In other words, in case of a fully developed wind sea, SAR imaging is highly nonlinear for $U_{10} \leq 13.5$ m s^{-1}.

For $\bar{c} = 2\pi$ the peak of the image spectrum is located at D.C. ($k = 0$ m^{-1}). In this case no wave information can be extracted anymore from the image spectrum.

If the wave field is a narrow-band swell, then the spectral peak starts shifting toward lower azimuthal wave numbers for larger values of $\bar{c}$ as compared with the wind sea case. Higher-order peaks may occur in the image spectrum for sufficiently large values of $\bar{c}$. However, in actual SAR imagery these higher order peaks should in general disappear in the background noise because of their low spectral level.

An important consequence of this azimuthal wave number shift is that ocean waves, which travel at an intermediate angle between the azimuth and range direction, appear on the image as being rotated toward the range direction, since the range component is not affected.

SEASAT-SAR data analyzed recently by *Beal et al.* [this issue] seem to support this result from our SAR simulation studies.

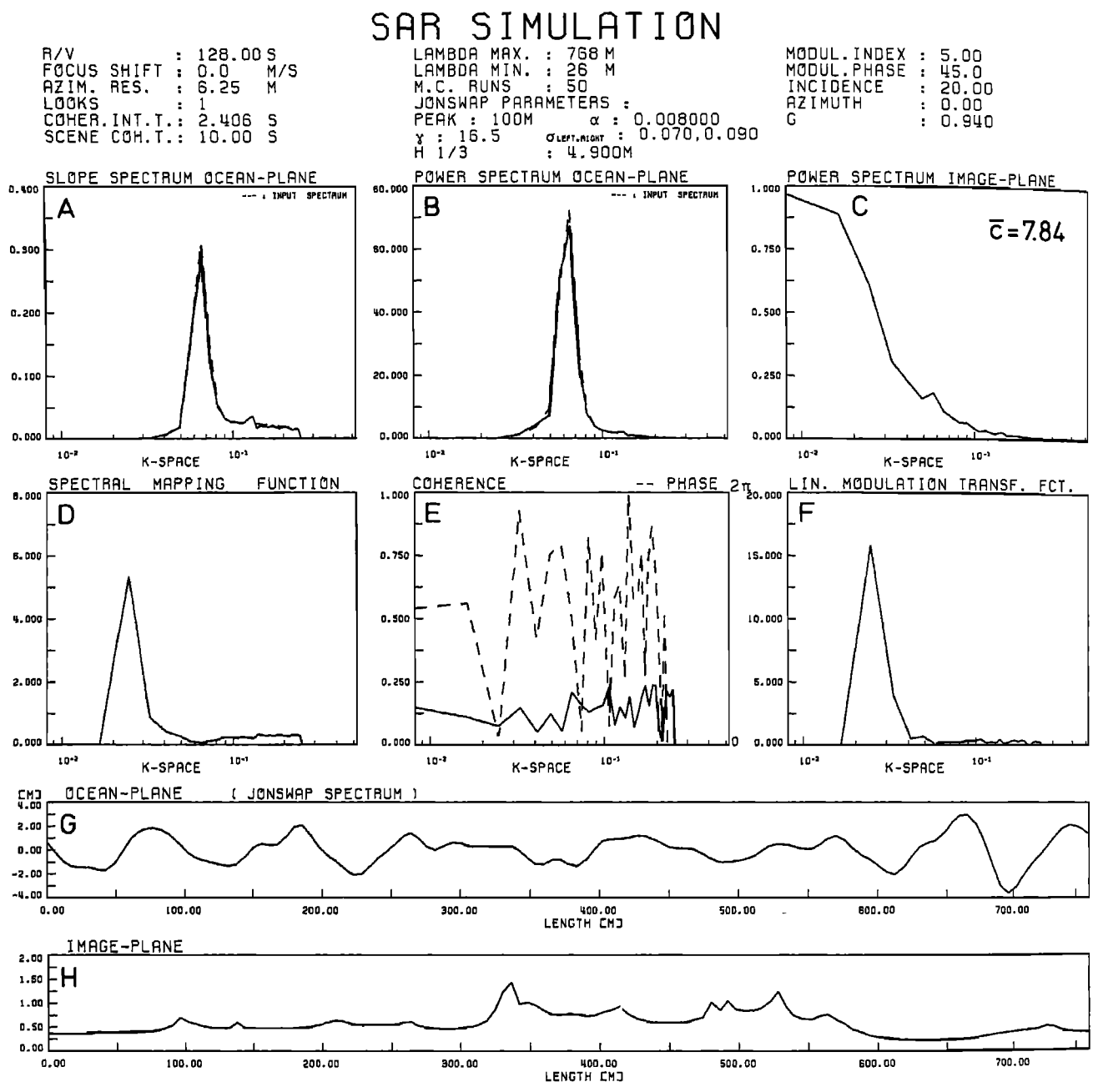

Fig. 12. SEASAT-SAR imaging of an azimuthally traveling swell of 100 m wavelength and 4.900 m significant wavelength.

Acknowledgments. This research has been sponsored by the Deutsche Forschungsgemeinschaft through the Sonderforschungsbereich 94, Meeresforschung Hamburg. I thank J. Szonn for implementing the program on the Cyber 173 computer and J. Schröter for his valuable advice.

REFERENCES

Alpers, W., and K. Hasselmann, The two-frequency technique for measuring ocean wave spectra from an airplane or satellite (Appendix B), *Boundary Layer Meteorol., 13,* 215–230, 1978.

Alpers, W. R., and C. L. Rufenach, The effect of orbital motions on synthetic aperture radar imagery of ocean waves, *IEEE Trans. Antennas Propagat., AP-27,* 685–690, 1979.

Alpers, W. R., D. B. Ross, and C. L. Rufenach, On the detectability of ocean surface waves by real and synthetic aperture radar, *J. Geophys. Res., 86,* 6481–6498, 1981.

Alpers, W., and K. Hasselmann, Spectral signal to clutter and thermal noise properties of ocean wave imaging synthetic aperature radars, submitted to *Int. J. Remote Sensing,* 1982.

Beal, R. C., D. G. Tilley, and F. M. Monaldo, Large- and small-scale spatial evolution of digitally processed ocean wave spectra from SEASAT synthetic aperture radar, *J. Geophys. Res.,* this issue.

Bendat, J. S., and A. G. Piersol, *Measurement and Analysis of Random Data,* John Wiley, New York, 1966.

Elachi, C., and W. E. Brown, Models of radar imaging of ocean surface waves, *IEEE Trans., AP-25,* 84–95, 1977.

Gonzales, F. I., R. C. Beal, W. E. Brown, P. S. DeLeonibus, J. W. Sherman III, J. F. R. Gower, D. Lichy, D. B. Ross, C. L. Rufenach, and R. A. Shuchman, SEASAT synthetic aperture radar: Ocean wave detection capabilities, *Science, 204,* 1418–1421, 1979.

Harger, R. O., The synthetic aperture radar image of time-variant scenes, *Radio Sci., 15,* 749–756, 1980.

Hasselmann, K., T. P. Barnett, E. Bouws, H. Carlson, D. E. Cartwright, K. Enke, J. A. Ewing, H. Gienapp, D. E. Hasselmann, P. Krusemann, A. Meerburg, P. Müller, D. J. Olbers, K. Richter, W. Sell, and H. Walden, Measurements of Wind-Wave Growth and Swell Decay During the Joint North Sea Wave Project (JONSWAP), *Deut. Hydrogr. Z., 8 (suppl. A.),* 1973.

Hasselmann, K., D. B. Ross, P. Müller, and W. Sell, A parametrical wave prediction model, *J. Phys. Oceanogr., 6,* 201–228, 1976.

Jain, A., Focussing effects in synthetic aperture radar imaging of ocean waves, *Appl. Phys., 15,* 323–333, 1978.

Jordan, R. L., The SEASAT-A synthetic aperture radar system, *IEEE J. Oceanic Eng., OE-5,* 154–164, 1980.

Kasischke, E. S., Extraction of gravity wave information from spaceborne synthetic aperture radar data, Master thesis, Univ. of Mich., Ann Arbor, 1980.

Larson, T. R., L. I. Moskowitz, and J. W. Wright, A note on SAR imagery of the ocean, *IEEE Trans. Antennas Propagat., AP-24,* 393–394, 1976.

Raney, R. K., Synthetic aperture imaging radar and moving targets, *IEEE Trans. Aerosp. Electr. Sys., AES-7,* 499–505, 1971.

Raney, R. K., SAR response to partially coherent phenomena, *IEEE Trans. Antennas Propagat., AP-28,* 777–787, 1980.

Raney, R. K., Wave orbital velocity, fade and sar response to azimuth waves, *J. Oceanic Eng., OE-6,* 140–146, 1981.

Raney, R. K., and R. T. Lowry, Ocean wave imagery and wave spectra distortion by synthetic aperture radar, in *Proceedings 12th International Symposium on Remote Sensing of Environment, Manila, Phillippines,* pp. 683–702, Environment Research Institute of Michigan, Ann Arbor, 1978.

Raney, R. K., and R. A. Shuchman, SAR mechanisms for imaging waves, paper presented at Proceedings of the 5th Canadian Symposium on Remote Sensing, Victoria, B. C., Canada, Aug. 1978.

Rufenach, C.L., and W. R. Alpers, Imaging ocean waves by synthetic aperture radars with long integration times, *IEEE Trans. Antennas Propagat., AP-29,* 422–428, 1981.

Swift, C. T., and L. R. Wilson, Synthetic aperture radar imaging of ocean waves, *IEEE Trans. Antennas Propagat., AP-27,* 725–729, 1979.

Tomiyasu, K., Ocean wave cross radial image error in synthetic aperture radar due to radial velocity, *J. Geophys. Res. 80,* 45–55, 1975.

Valenzuela, G. R., An asymptotic formulation for SAR images of the dynamical ocean surface, *Radio Sci., 15,* 105–114, 1980.

Wright, J. W., W. J. Plant, W. C. Keller, and W. L. Jones, Ocean wave radar modulation transfer functions from the West Coast Experiment, *J. Geophys. Res., 85,* 4957–4966, 1980.

(Received January 25, 1982;
revised July 21, 1982;
accepted July 21, 1982.)